Please do not adjust margins

ARTICLE

$Na_2B_{11}H_{13}$ and $Na_{11}(B_{11}H_{14})_3(B_{11}H_{13})_4$ as Potential Solid-State Electrolytes for Na-Ion Batteries†

Received 00th January 20xx,
Accepted 00th January 20xx

DOI: 10.1039/x0xx00000x

Diego H. P. Souza,[a] Anita M. D'Angelo,[b] Terry D. Humphries,[a] Craig E. Buckley,[a] and Mark Paskevicius[a*]

Solid-state sodium batteries have attracted great attention owing to their improved safety, high energy density, large abundance and low cost of sodium compared to current Li-ion batteries. Sodium-boranes have been studied as potential solid-state electrolytes and the search for new materials is necessary for future battery applications. Here, a facile and cost-effective solution-based synthesis of $Na_2B_{11}H_{13}$ and $Na_{11}(B_{11}H_{14})_3(B_{11}H_{13})_4$ is demonstrated. $Na_2B_{11}H_{13}$ presents an ionic conductivity in the order of 10^{-7} S cm^{-1} at 30 °C, but undergoes an order-disorder phase transition and reaches 10^{-3} S cm^{-1} at 100 °C, close to that of liquids and the solid-state electrolyte Na-*β*-Al_2O_3. The formation of the mixed-anion solid-solution, $Na_{11}(B_{11}H_{14})_3(B_{11}H_{13})_4$, partially stabilises the high temperature structural polymorph observed for $Na_2B_{11}H_{13}$ to room temperature and it exhibits Na^+ conductivity higher than its constituents (4.7 x 10^{-5} S cm^{-1} at 30 °C). $Na_2B_{11}H_{13}$ and $Na_{11}(B_{11}H_{14})_3(B_{11}H_{13})_4$ exhibit an oxidative stability limit of 2.1 V vs. Na^+/Na.

Introduction

Hydridoborates compounds have attracted the interest of researchers in the past decades due to their rich chemistry and variety of compositions and structures.[1,2] These compounds have shown applicability in a number of different fields, such as medicinal chemistry,[3] military,[4] organic synthesis,[5,6] hydrogen storage[7–9] and as ionic conductors.[10,11]

Closo-boranes, negatively charged hydridoborate clusters with a cage-like structure, form metal salts with high chemical and thermal stability as well as superionic conductivity of their respective metal cations at high temperatures.[12–15] Generally, these compounds undergo an order-disorder polymorphic phase transition at a specific temperature, which results in fast anion reorientational dynamics and high cation mobility.[16,17] Several attempts to improve the performance of hydridoborate salts as solid-state electrolytes at room temperature have been reported, such as chemical modification of the anion,[12,15,18] mechanical-induced modification,[19–21] and anion mixtures with other borane compounds[22–24] or metal oxides.[25,26] These strategies seem to create defects into the structure and/or stabilise the disordered high temperature polymorph to room temperature, which increases the ionic conductivity of the material.[21,22] Recently, *nido*-boranes, boron anions with a nest-like open-cage structure, have also been investigated as potential solid-state electrolytes due to their high ionic conductivity properties at room temperature.[11,27–29]

The use of inorganic salts, such as metal boranes, as solid electrolytes seems to be an attractive choice for the development of solid-state batteries, which promise high energy storage capacity, durability and safety, with the elimination of the flammable organic liquid electrolyte used in current generation Li-ion batteries.[16,30] The energy density of a battery cell can be increased with the use of solid electrolytes, as they can be more compatible with alternative electrode materials, e.g. pure lithium or sodium metal.[30,31] Lithium-ion batteries are one of the most common types of energy storage technology, and they are used in a variety of electronic devices. However, the increasing use of lithium will limit its availability and raise its cost, which makes it necessary to search for alternative metal-ion battery technologies.[32] This is exemplified by the recent ≈ 500% increase in Li metal prices in a single year, due to rapidly rising electric vehicle demand.[33] Moreover, a conservative lithium consumption forecast, based only on the increasing demand from electric vehicles, shows that the lithium reserve on land will be totally consumed in about 60 years.[34]

It has been observed that certain sodium borane salts exhibit even higher ionic conductivities than their lithium borane analogues at room temperature.[11,15,27] Na-batteries are being actively investigated as sodium metal is more abundant than lithium, has a lower cost, and presents a suitable standard half-cell potential (−2.71 V vs. standard hydrogen electrode).[32,35,36] Current sodium-sulphur (Na−S) batteries operate with molten electrodes using a solid-electrolyte, sodium *β*-alumina ($NaAl_{11}O_{17}$).[37] However, operation is required to occur at high temperatures (300 – 350 °C), which incurs safety issues, limits scalability, and presents higher operating costs. Some of the

[a.] *Department of Physics and Astronomy, Curtin University, GPO Box U1987, Perth, WA 6845, Australia.*
[b.] *Australian Synchrotron (ANSTO), Clayton, VIC 3168, Australia.*

† Electronic Supplementary Information (ESI) available: Solution-state and solid-state NMR, XRPD, DSC/TGA, and LSV data. Rietveld refinements, Nyquist and ionic conductivity plots. Supplementary table. See DOI: 10.1039/x0xx00000x

Please do not adjust margins

Please do not adjust margins

difficulties surrounding the implementation of room temperature Na–S batteries can be avoided by searching for a solid-state alternative to problematic liquid electrolytes.[37,38] Due to the promising properties observed for some sodium *nido*-boranes as solid-state electrolytes,[11,27,29] the synthesis and characterisation of $Na_2B_{11}H_{13}$ is investigated, as well as the mixed-anion solid solution $Na_{11}(B_{11}H_{14})_3(B_{11}H_{13})_4$.

Experimental section

Chemicals

Sodium borohydride ($NaBH_4$, anhydrous, 98%), diglyme ($C_6H_{14}O_3$, anhydrous, 99.5%), 1-bromopentane ($C_5H_{11}Br$, 98%), diethyl ether ($(C_2H_5)_2O$, anhydrous, 99.7%), trimethylamine hydrochloride ($(CH_3)_3N{\cdot}HCl$, 98%), deuterated water (D_2O, 99.9 atom % D), sodium (Na lump in kerosene, 99%), graphite powder (C, 99.9%), tetrahydrofuran (THF, with 250 ppm BHT, 99%), sodium hydride (NaH, 90%), sodium hydroxide (NaOH, 98%) and platinum foil (Pt, 99.95%, thickness 0.1 mm) were all purchased from Sigma-Aldrich. Gold foil (Au, 99.95%, thickness 0.1 mm) was obtained from Alfa Aesar, and acetone (C_3H_6O, 99.5%) from Unilab. To maintain an inert atmosphere, all chemicals and samples were manipulated in an argon filled glovebox (Mbraun, O_2 & H_2O < 1 ppm) or using Schlenk techniques under argon.

Nuclear Magnetic Resonance (NMR) Spectroscopy

Powdered samples were characterised through ^{11}B (128 MHz) solid-state NMR spectroscopy with a Varian VNMRS 400 NMR spectrometer at room temperature. The samples (≈ 30 mg) were ground using a mortar and pestle and packed inside a 4 mm zirconia rotor in an argon filled glovebox and sealed with a gas-tight insert. The samples were spun at 5 kHz, and acquisition was performed with proton decoupling and a one pulse sequence, with a relaxation delay of 10 s for a total of 50 transients.

Solution-state NMR spectroscopy was also used to characterise samples with a Bruker Avance III 400 MHz NanoBay spectrometer. ^1H: 400 MHz, ^{11}B: 128 MHz, $^{11}B\{^1H\}$: 128 MHz NMR data were collected after dissolution of the solids in 600 µL of deuterated water (D_2O). The ^{11}B NMR spectra were referenced to a boron trifluoride etherate ($BF_3O(C_2H_5)_2$) external standard, and the ^1H NMR spectra were referenced to a tetramethylsilane ($Si(CH_3)_4$) external standard.

Structural Characterisation

X-Ray Powder Diffraction (XRPD) data were acquired by employing a Bruker D8 Advance Powder Diffractometer with a Cu K_α radiation source (λ = 1.54056 Å) operated at 40 kV/40 mA with a LynxEye detector in the 2ϑ range of 5 – 60°. The samples were ground using a mortar and pestle in an argon filled glovebox, mounted on a single-crystal Si low background sample holder and sealed with an airtight poly(methyl-methacrylate) (PMMA) dome under argon to prevent air exposure during data collection. The use of the dome results in two broad diffraction halos at low angle.

The sample $Na_2B_{11}H_{13}$ was characterised using Synchrotron Radiation X-Ray Powder Diffraction (SR-XRPD) at the Australian Synchrotron Powder Diffraction beamline (λ = 0.590827(4) Å) and refined using a NIST LaB_6 660b line position standard. The solid was ground using a mortar and pestle and packed inside a 1.0 mm borosilicate capillary inside an argon filled glovebox, which was then flame-sealed. A Mythen II microstrip detector was used to collect the data at two positions from 1° – 81° 2ϑ (0.0038° steps),[39] which were merged into gap-free data sets. *In-situ* SR-XRPD experiments were performed under heating ($\Delta T/\Delta t$ = 5 °C min^{-1}) and cooling ($\Delta T/\Delta t$ = 6 °C min^{-1}) from 30 – 230 – 30 °C, which was controlled by an Oxford Cryosystems Cryostream Plus using a 60 s data collection time for each scan. Rietveld refinement of diffraction patterns was conducted using Bruker Topas software (version 5),[40] and reported uncertainties are based on mathematical fitting uncertainty in the Topas software. Rietveld refinements were conducted using a Le Bail model for the identification of phases, but no atomic information was used.

Differential Scanning Calorimetry and Thermogravimetric analysis (DSC/TGA)

Thermal behaviour was analysed using a Netzsch STA 449 F3 Jupiter DSG/TGA. The powders were ground with a mortar and pestle inside an argon filled glovebox, and approximately 5 mg of each sample was mounted inside an Al crucible and crimp-sealed with a lid. The lid was pierced (≈ 10 seconds prior to analysis), and the crucible was transferred to the Pt furnace, which was evacuated and filled with argon (40 mL min^{-1}). The data were obtained from 40 – 350 °C at 10 °C min^{-1}. The sample $Na_2B_{11}H_{13}$ was also analysed under heating and cooling from 40 – 220 – 40 °C under the same conditions already described. The temperature and sensitivity of the DSC/TGA was calibrated using In, Zn, Sn, Bi and CsCl reference materials, resulting in a temperature accuracy of ± 0.2 °C, while the balance has an accuracy of ± 20 µg.

Electrochemical Impedance Spectroscopy (EIS)

Solid-state ionic conductivity measurements were collected as a function of temperature by using a ZIVE SP1 electrochemical workstation at 100 mV AC from 10 Hz to 1 MHz at RT (room temperature) and isothermally after heating with 50 minutes of thermal equilibrium at each 10 °C temperature step. $Na_2B_{11}H_{13}$ was analysed from 30 – 200 °C, and 30 – 170 °C for $Na_{11}(B_{11}H_{14})_3(B_{11}H_{13})_4$. The samples were ground with a mortar and pestle inside an argon filled glovebox, and approximately 30 mg of each sample was pressed into pellets (6 mm diameter) at 700 MPa between two gold foils (0.1 mm thickness). They were sealed within an air-tight 'Swagelok-type' Teflon cell with 316 stainless steel electrodes. The temperature was recorded using a K-type thermocouple, which was placed ≈ 5 mm from the pellet inside a sealed tube furnace. The Nyquist plots at low temperature were fitted using the equivalent circuit model (R_1 + Q_1)/(R_2 + W_o), in which R_1 is the internal resistance, R_2 the charge transfer resistance, Q_1 is the constant phase element and W_o is the Warburg element to obtain the impedance of the pellet.[41] At high temperatures, due to the absence of the semi-circle at high and intermediate frequencies, the pellet impedance was determined through the intercept of the linear spike with the *x*-axis in the Nyquist plots.[41]

This journal is © The Royal Society of Chemistry 20xx

Please do not adjust margins

Please do not adjust margins

Solid-state ionic conductivity data (σ) were determined from: $\sigma = d/lA$, where σ is the ionic conductivity in S cm^{-1}, d is the pellet thickness in cm, l is the x-intercept of the Nyquist blocking tail (pellet impedance), and A is the area of the pellet face in cm^2.
The activation energy of each material was determined from the slope of the solid-state ionic conductivity plot between 30 – 50 °C for LT (low temperature) $Na_2B_{11}H_{13}$, 170 – 190 °C for HT (high temperature) $Na_2B_{11}H_{13}$ and 30 – 80 °C for $Na_{11}(B_{11}H_{14})_3(B_{11}H_{13})_4$ using the logarithm of the Arrhenius equation: $\ln \sigma_{ion} = \ln \sigma_o - (E_a/K_BT)$, where σ_o is a pre-exponential factor (S cm^{-1}), E_a the activation energy (J), K_B Boltzmann's constant (1.3806 x 10^{-23} J K^{-1}), and T the temperature (K).[11,42]

Linear Sweep Voltammetry (LSV)

A mixture of 75(SSE):25(graphite), where SSE = $Na_2B_{11}H_{13}$ or $Na_{11}(B_{11}H_{14})_3(B_{11}H_{13})_4$ was prepared by grinding in a mortar and pestle repeatedly until a fine mixture was obtained. Graphite was previously dried under vacuum at 550 °C for 12 hours to remove any moisture or volatiles. 2.5 mg of that mixture was layered on top of 28 mg of SSE and pressed at 700 MPa to form a pellet that was sandwiched between aluminium, platinum and sodium foil in the following configuration (Al/Pt/SSE+C/SSE/Na), which was then sealed within an air-tight 'Swagelok-type' Teflon cell with stainless steel electrodes. LSV was conducted from 1.4 – 6.0 V at 30 °C with a scan rate of 50 µV s^{-1}. The oxidative stability voltage limit of each sample was determined from the intersection point of the regression lines ($R^2 > 0.99$) fitted to the background and anodic currents in the voltammogram following a known method.[43]

Synthesis of mixed anion *nido*-borane, $Na_{11}(B_{11}H_{14})_3(B_{11}H_{13})_4$

The synthesis of $Na_{11}(B_{11}H_{14})_3(B_{11}H_{13})_4$ was achieved through the reaction of $(CH_3)_3NHB_{11}H_{14}$ with NaOH, according to reaction 1.

$$7\ (CH_3)_3NHB_{11}H_{14(aq)} + 11\ NaOH_{(aq)} \xrightarrow{H_2O,\ 100\ ^\circ C} Na_{11}(B_{11}H_{14})_3(B_{11}H_{13})_{4(aq)} + 7\ (CH_3)_3N_{(g)} + 11\ H_2O_{(l)} \quad (1)$$

$(CH_3)_3NHB_{11}H_{14}$ was prepared based on the same methodology described in our previous work.[11] The trimethylammonium-borane salt was recrystallised prior to use by solubilisation in a hot aqueous solution of acetone (10% acetone).[44] The colourless powder of $(CH_3)_3NHB_{11}H_{14}$ that was obtained was filtered and dried under vacuum at 90 °C before use. 400 mg of recrystallised $(CH_3)_3NHB_{11}H_{14}$ (2.1 mmol) was dissolved into 20 mL of an aqueous solution of 177 mg of NaOH (4.4 mmol, ≈ 33% excess), which was then heated at 100 °C for 15 minutes under constant stirring in an open vessel. After cooling back to room temperature, the solution was filtered, and the filtrate was washed three times with 5 mL of diethyl ether.
The aqueous layer was dried *in vacuo* at 110 °C overnight, and a solid containing a mixture of both anions was obtained (0.28 g, 0.24 mmol, 80% yield). No additional step for removal of excess NaOH or possible by-products was taken.

Synthesis of disodium *nido*-tridecahydroundecaborane, $Na_2B_{11}H_{13}$

The synthesis of $Na_2B_{11}H_{13}$ was achieved based on reaction 2, an adapted procedure proposed by Pecyna *et. al.*[45] that was originally used to prepare $(C_2H_5)_4NCB_{11}H_{12}$.

$$(CH_3)_3NHB_{11}H_{14(sol)} + 2\ NaH_{(s)} \xrightarrow{THF} Na_2B_{11}H_{13(s)} + (CH_3)_3N_{(g)} + 2\ H_{2(g)} \quad (2)$$

0.11 g of NaH (4.6 mmol) was mixed with 5 mL of THF under argon in an ice bath. Under constant stirring, 5 mL of a THF solution containing 250 mg of recrystallised $(CH_3)_3NHB_{11}H_{14}$ (1.3 mmol) was added slowly and left stirring for 15 minutes at 0 °C and for 30 minutes at room temperature. The mixture was filtered, and the filtrate was dried *in vacuo* at 40 °C for 2 hours, which yielded a white powder of $Na_2B_{11}H_{13}$ (0.17 g, 0.9 mmol, 73% yield).

Results and discussion

Sample characterisation

Solid-state ^{11}B MAS NMR spectroscopy was used to identify the composition of each material synthesised in the powdered state (Fig. 1). $NaB_{11}H_{14}\cdot(H_2O)_n$, reported in our previous work,[11] was also characterised and added for comparison.
The resonances at δ^{11}B −15.2 and −17.9 ppm are assigned to $B_{11}H_{14}^-$,[29] whereas $B_{11}H_{13}^{2-}$ is represented by the signals at δ^{11}B −21.5 and −32.2 ppm.[11] $B_{11}H_{13}^{2-}$ resonances cannot be observed in the spectra of hydrated $NaB_{11}H_{14}$ samples, and there is no apparent signal of $B_{11}H_{14}^-$ in the sample of $Na_2B_{11}H_{13}$. The asymmetry of the main peak in the $Na_2B_{11}H_{13}$ pattern (δ^{11}B −21.5 ppm) may indicate that some $NaB_{11}H_{14}$ could exist in that powder, however an analysis of solution-state ^{11}B NMR of $Na_2B_{11}H_{13}$ in D_2O also does not show any presence of $B_{11}H_{14}^-$ peaks (Fig. S1). The only material that shows the presence of

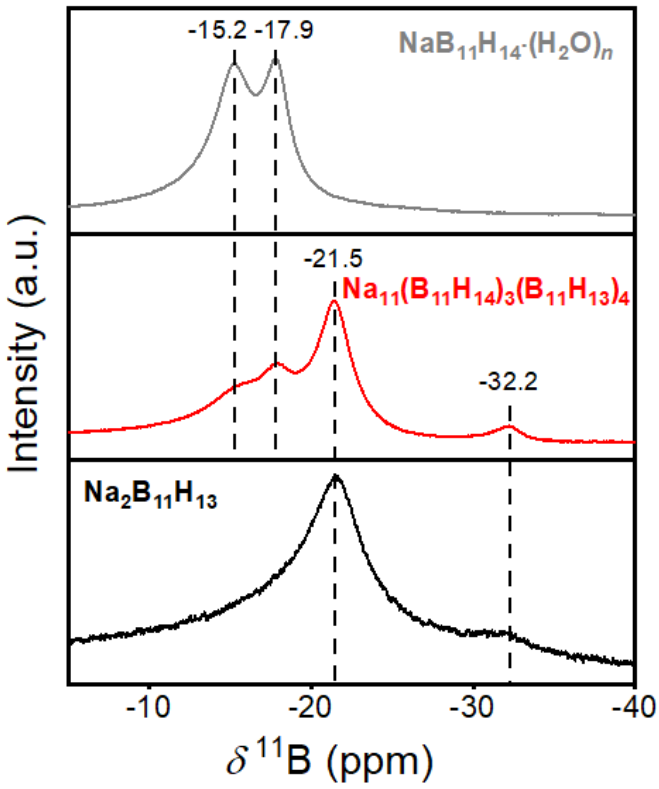

Fig. 1. Solid-state ^{11}B MAS NMR spectra of $NaB_{11}H_{14}\cdot(H_2O)_n$, $Na_{11}(B_{11}H_{14})_3(B_{11}H_{13})_4$ and $Na_2B_{11}H_{13}$ at room temperature. δ ($B_{11}H_{14}^-$) = −15.2 and −17.9 ppm, and δ ($B_{11}H_{13}^{2-}$) = −21.5 and −32.2 ppm.

Please do not adjust margins

Please do not adjust margins

both anions in the solid-state is $Na_{11}(B_{11}H_{14})_3(B_{11}H_{13})_4$, which consists of 0.75 mol of $B_{11}H_{14}^-$ to 1 mol of $B_{11}H_{13}^{2-}$ based on the integration of the solid-state NMR resonances. However, it is interesting that when $Na_{11}(B_{11}H_{14})_3(B_{11}H_{13})_4$ is dissolved in D_2O and analysed through solution-state ^{11}B NMR, the integration of the NMR signals provides a composition of 0.13 mol of $B_{11}H_{14}^-$ to 1 mol of $B_{11}H_{13}^{2-}$ (Fig. S1). The observation of less $B_{11}H_{14}^-$ in the solution-state ^{11}B NMR spectrum of $Na_{11}(B_{11}H_{14})_3(B_{11}H_{13})_4$ could be due to the deprotonation of this anion into $B_{11}H_{13}^{2-}$ in an alkaline medium as follows:[11,28]

$$B_{11}H_{14}^-{}_{(aq)} + OH^-{}_{(aq)} \rightleftarrows B_{11}H_{13}^{2-}{}_{(aq)} + H_2O_{(l)} \quad (3)$$

During synthesis, excess NaOH was not specifically removed, which could remain to some degree within the solid product, however the XRPD pattern for $Na_{11}(B_{11}H_{14})_3(B_{11}H_{13})_4$ (Fig. 2 & S2) does not show any presence of unreacted NaOH, which instead suggests the formation of an amorphous sodium borate, which could be alkaline on dissolution.[46–48] The diffractogram of $Na_2B_{11}H_{13}$ also does not show any presence of unreacted NaH (Fig. 2 & S2), which implies that all the excess starting material used was successfully removed through filtration.

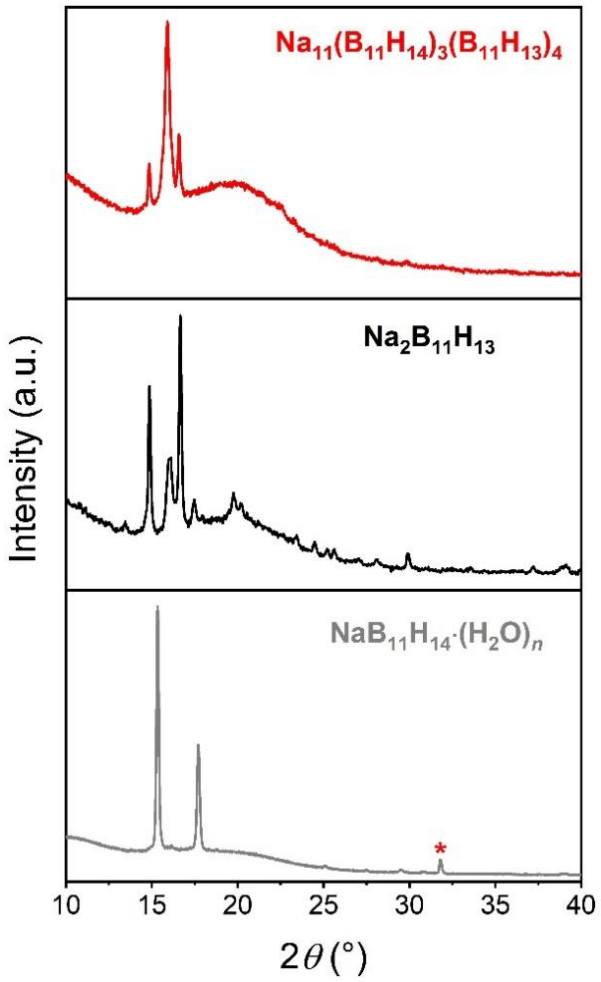

Fig. 2. XRPD pattern (λ = 1.54056 Å) for $Na_{11}(B_{11}H_{14})_3(B_{11}H_{13})_4$, $Na_2B_{11}H_{13}$ and $NaB_{11}H_{14}\cdot(H_2O)_n$[11] (added for comparison) at room temperature. Asterisk at 2Θ = 31.8° in the $NaB_{11}H_{14}\cdot(H_2O)_n$ pattern represent inadvertent NaCl contamination from synthesis.[11]

The possibility of alkaline aqueous solutions upon dissolution of $Na_{11}(B_{11}H_{14})_3(B_{11}H_{13})_4$ can be elucidated by analysing the NMR data in more detail. Solid-state ^{11}B MAS NMR spectroscopy of $Na_{11}(B_{11}H_{14})_3(B_{11}H_{13})_4$ (Fig. S3) shows the presence of small resonances at ≈ +1 ppm and between +10 and +22 ppm, which represent BO_4 and BO_3 units, respectively, of an inorganic borate[49–51], e.g. hydrated sodium metaborate, $NaB(OH)_4$.[47,52,53] It has been reported that the reaction of $(CH_3)_3NHB_{11}H_{14}$ with a metal hydroxide in aqueous solution under heating yields boric acid as a side product.[11] Sodium metaborate can then be formed by the reaction of boric acid with excess NaOH.[54,55] In aqueous solution, $NaB(OH)_4$ dissociates, releasing NaOH and yielding a solution with a high pH, which induces deprotonation of $B_{11}H_{14}^-$ into $B_{11}H_{13}^{2-}$ (reactions 3 and 4),[11,28,54,55] and formation of boric acid, which is observed in the ^{11}B solution-state NMR of $Na_{11}(B_{11}H_{14})_3(B_{11}H_{13})_4$ in D_2O at 14.6 ppm (Fig. S1).

$$NaB(OH)_{4(aq)} \rightleftarrows NaOH_{(aq)} + H_3BO_{3(aq)} \quad (4)$$

As such, it is postulated that $Na_{11}(B_{11}H_{14})_3(B_{11}H_{13})_4$ contains some quantity of $NaB(OH)_4$ (≈ 8 mol% based on integration of the MAS NMR resonances), or a derivative thereof, that only affects the structure of the undecaborane upon aqueous dissolution. It should be highlighted that it is critical to characterise *nido*-borane anions through solid-state ^{11}B MAS NMR, as the results of solution-state NMR can be misleading due to possible side reactions upon dissolution. This has also been a problem identified in NMR studies of higher boranes formed during metal borohydride decomposition.[56] The specific issue faced with impurities in $Na_{11}(B_{11}H_{14})_3(B_{11}H_{13})_4$ may also be solved by the removal of the inorganic borate from solution, however, in the case of $Na_{11}(B_{11}H_{14})_3(B_{11}H_{13})_4$, the separation of a borate species from a sample that contains $Na_2B_{11}H_{13}$ can be challenging as both have strong polar features and similar solubility properties in polar and apolar solvents. Prior to drying, the aqueous solution of $Na_{11}(B_{11}H_{14})_3(B_{11}H_{13})_4$ was washed three times with diethyl ether, as an attempt to remove impurities and isolate both anions, $B_{11}H_{14}^-$ and $B_{11}H_{13}^{2-}$, from the medium. However, upon drying the aqueous layer, a solid was obtained that was a mixture of both anions and the inorganic borate.

The ^1H solution-state NMR of $Na_2B_{11}H_{13}$ in D_2O shows the presence of THF (Fig. S4), which accounts for only 0.15 mol of THF to 1 mol of $Na_2B_{11}H_{13}$ based on the integration of the NMR resonances. The multiplets at 1.7 and 3.6 ppm represent the resonances of CH_2 and CH_2O from THF, respectively,[57,58] and those between −0.6 and 1.5 ppm were assigned to $B_{11}H_{13}^{2-}$. $Na_2B_{11}H_{13}$ was only briefly dried at 40 °C during synthesis to avoid unwanted decomposition, which may allow some THF to remain coordinated to the dried solid.

$Na_2B_{11}H_{13}$ was also analysed through *in-situ* SR-XRPD and DSC (Fig. 3), and it can be seen that a polymorphic phase transition occurs at ≈ 170 °C upon heating (endothermic) and 90 °C on cooling (exothermic). Another endothermic event, between 60 – 90 °C, can be identified during heating in the DSC (Fig. 3) and DSC/TGA (Fig. S5) plots with a subsequent mass loss of 5.5(2) wt%, which accounts for the release of residual coordinated THF. This mass loss is in close agreement with the amount of

This journal is © The Royal Society of Chemistry 20xx

Please do not adjust margins

Please do not adjust margins

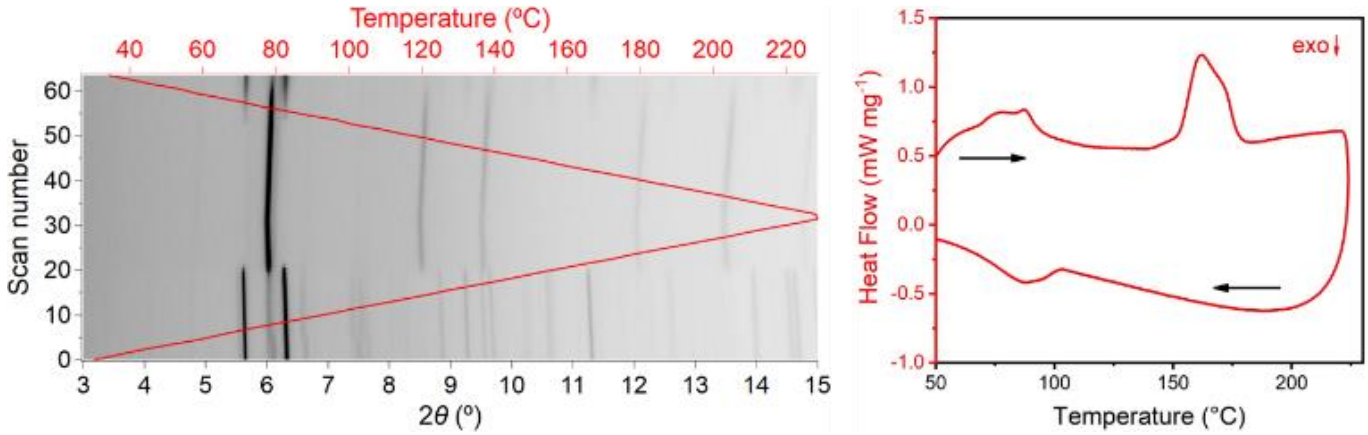

Fig. 3. Left: *In-situ* SR-XRPD data (λ = 0.590827(4) Å) of $Na_2B_{11}H_{13}$ during heating (5 °C min^{-1}) and cooling (6 °C min^{-1}). A reversible polymorphic phase transition is seen at ≈ 170 °C on heating and 90 °C on subsequent cooling. Red line represents temperature. Right: DSC plot ($\Delta T/\Delta t$ = 10 °C min^{-1}, Ar flow = 40 mL min^{-1}) for $Na_2B_{11}H_{13}$ upon heating and cooling between 40 and 220 °C.

THF that was calculated through integration of the ^{1}H NMR peaks (Fig. S4), which corresponds to 0.15 mol of THF to 1 mol of $Na_2B_{11}H_{13}$. A mass loss of 3.1(2) wt% observed between 320 and 340 °C (Fig. S5) is assigned to the decomposition of the sample, commensurate with a large exothermic feature. The decomposition temperatures of other *nido*-boranes, such as $LiB_{11}H_{14}\cdot(H_2O)_n$, $NaB_{11}H_{14}\cdot(H_2O)_n$ and $KB_{11}H_{14}$ have already been identified to be ≈ 210 °C with a sharp exothermic peak in their DSC/TGA plot coupled with hydrogen release.[11] Solution-state ^{1}H NMR spectroscopy of $Na_2B_{11}H_{13}$ after DSC/TGA, in which the sample was heated to 220 °C and cooled back to room temperature, reveals that THF resonances are no longer detected (Fig. S6). However, the ^{11}B NMR spectrum does reveal a 5 mol% impurity of $B_{11}H_{14}^-$ that is present after heating.

Fig. 4 shows select SR-XRPD diffractograms of $Na_2B_{11}H_{13}$ at different temperatures during and after heating. No major differences can be observed between the diffractogram at 30 °C (before heating) and after the minor THF release. This implies that the small amount of THF detected in the sample (0.15 mol of THF to 1 mol of $Na_2B_{11}H_{13}$) could be solvent adsorbed to the powder, or that the material is composed of a mixture of $Na_2B_{11}H_{13}$ and $Na_2B_{11}H_{13}\cdot(THF)_x$. The THF is considered a small impurity, and the sample is here called $Na_2B_{11}H_{13}$. Samples of $Na_2B_{11}H_{13}$ can then be prepared THF free by disolvating the powder under vacuum at slightly higher temperatures than the one here adopted (40 °C) without its decomposition.

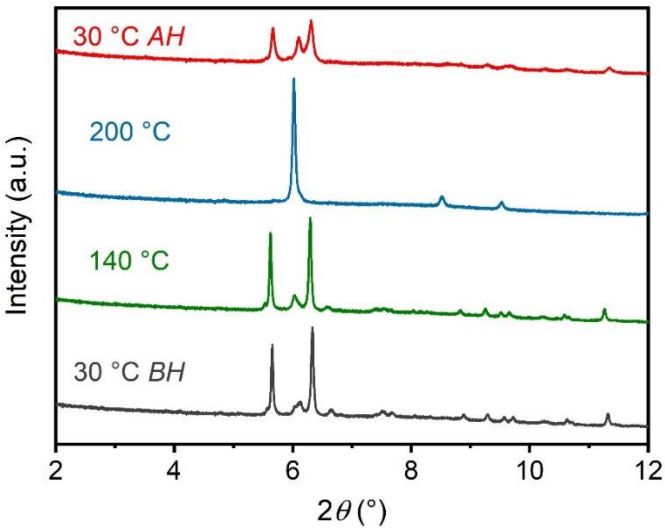

Fig. 4. SR-XRPD patterns (λ = 0.590827(4) Å) for $Na_2B_{11}H_{13}$ at 30 °C *BH* (before heating), 30 °C *AH* (after heating), 140 °C and 200 °C (during *in-situ* heating experiment).

At 200 °C, $Na_2B_{11}H_{13}$ has completely undergone a polymorphic phase change, assuming a disordered body-centered cubic (bcc) structure, indexed in $Pm\overline{3}n$ with a = 7.955(1) Å and V = 503.32(2) Å^3 (Fig. S7). This is the same symmetry observed for the high temperature $Na_2B_{12}H_{12}$, which undergoes the first polymorphic transition near 257 °C.[59] After cooling from 220 °C to 30 °C after heating, the SR-XRPD (Fig. 4) shows that the HT polymorph is only metastable and is predominantly transformed back into the original structure, with a minor portion of the $Pm\overline{3}n$ phase remaining, as seen in Figs. 3 & 4.

Interestingly, there are similarities in the room temperature diffraction patterns of $Na_2B_{11}H_{13}$ after heating and $Na_{11}(B_{11}H_{14})_3(B_{11}H_{13})_4$, with the three main diffraction peaks located at Q = 1.05, 1.13 and 1.17 Å^{-1} in both diffractograms ($Q = (4\pi\sin\vartheta)/\lambda$, Fig. 5). In fact, the cubic $Pm\overline{3}n$ polymorph, represented by the peak at Q = 1.13 Å^{-1}, seems to be present in the diffractogram of both samples, $Na_2B_{11}H_{13}$ at RT after heating (*AH*) and $Na_{11}(B_{11}H_{14})_3(B_{11}H_{13})_4$ at RT, with greater intensity, relative to the peaks at Q = 1.05 and 1.17 Å^{-1}, in $Na_{11}(B_{11}H_{14})_3(B_{11}H_{13})_4$ than in $Na_2B_{11}H_{13}$. This is also shown in Fig. S8 where the $Pm\overline{3}n$ polymorph in $Na_2B_{11}H_{13}$ at 200 °C is refined to a = 7.955(1) Å and V = 503.32(2) Å^3 and in $Na_{11}(B_{11}H_{14})_3(B_{11}H_{13})_4$ at room temperature it is refined to a = 7.983(1) Å and V = 487.94(9) Å^3. The peaks observed at Q = 1.05 and 1.17 Å^{-1} represent the Bragg reflections from the low temperature structures of the sodium borane. These data suggest that samples of $Na_2B_{11}H_{13}$ and $Na_{11}(B_{11}H_{14})_3(B_{11}H_{13})_4$ have some degree of dynamics in their structures at room temperature, which is enhanced to a greater degree in the mixed anion compound.

The DSC/TGA plot for $Na_{11}(B_{11}H_{14})_3(B_{11}H_{13})_4$ (Fig. S9) shows a subtle endothermic event (≈ 160 °C) close to the temperature observed for $Na_2B_{11}H_{13}$ (170 °C), which may indicate the complete transformation to the same $Pm\overline{3}n$ polymorph seen in $Na_2B_{11}H_{13}$. Based on the XRPD data (Fig. 5), most of the sample

Please do not adjust margins

Please do not adjust margins

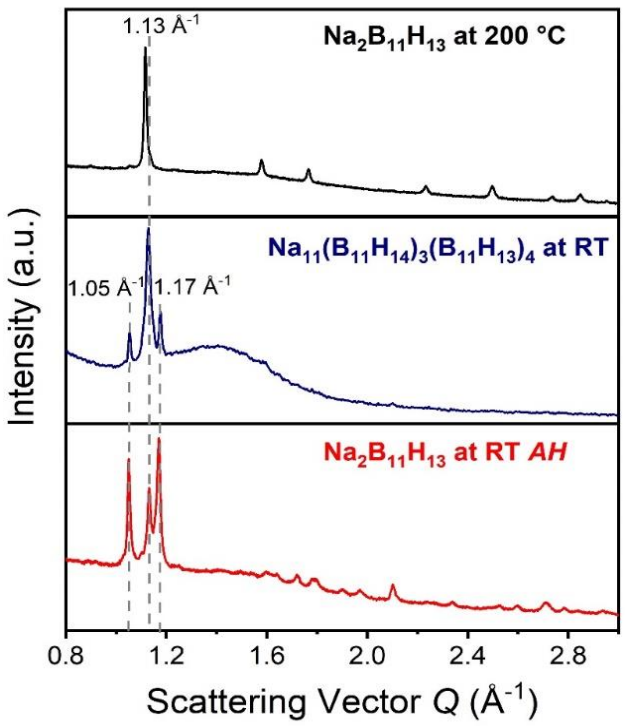

Fig. 5. XRPD pattern (λ = 1.54056 Å) for $Na_{11}(B_{11}H_{14})_3(B_{11}H_{13})_4$ at room temperature (blue), and SR-PXD data (λ = 0.590827(4) Å) for $Na_2B_{11}H_{13}$ at 200 °C (black) and at room temperature after being heated to 220 °C (red). Dashed lines at 1.05, 1.17 $Å^{-1}$ (RT polymorph) and at 1.13 $Å^{-1}$ (HT polymorph) were added to show the similarities between the diffractograms. The diffractograms were plotted with the *x*-axis in scattering vector to compare XRPD results obtained using different wavelengths.

$Na_{11}(B_{11}H_{14})_3(B_{11}H_{13})_4$ at RT is already in the *Pm*$\bar{3}$*n* polymorph, and it is surmised that the remaining portion of that sample would transition into this polymorph at 160 °C, which generates a discrete endothermic feature. $Na_{11}(B_{11}H_{14})_3(B_{11}H_{13})_4$ also exhibits an exothermic peak at 265 °C with a weight loss of 1.7(4) wt%, which indicates its decomposition.

Fig. S10 shows a comparison between the DSC results obtained for $NaB_{11}H_{14}\cdot(H_2O)_n$,[11] $Na_{11}(B_{11}H_{14})_3(B_{11}H_{13})_4$ and $Na_2B_{11}H_{13}$ from 50 – 350 °C. It is possible to observe that samples containing a larger proportion of $B_{11}H_{13}^{2-}$, rather than $B_{11}H_{14}^{-}$, exhibit a higher thermal stability, with elevated temperatures for their exothermic decomposition. This may be due to the fact that salts of $Na_2B_{11}H_{13}$ present higher lattice energy than salts of $NaB_{11}H_{14}$.[60,61]

Electrochemical Analysis

The solid-state Na^+ conductivity of $Na_{11}(B_{11}H_{14})_3(B_{11}H_{13})_4$ and $Na_2B_{11}H_{13}$ was investigated through AC impedance measurements as a function of temperature and compared to other single-anion and mixed-anion sodium hydridoborate salts and the solid-state electrolyte Na-*β*-Al_2O_3[1] (Fig. 6). For simplicity, an Arrhenius plot of ionic conductivity of $Na_{11}(B_{11}H_{14})_3(B_{11}H_{13})_4$ and $Na_2B_{11}H_{13}$ compared only to anhydrous and hydrated $NaB_{11}H_{14}$ was also plotted (Fig. S11). The Nyquist plots for $Na_2B_{11}H_{13}$ and $Na_{11}(B_{11}H_{14})_3(B_{11}H_{13})_4$ at certain temperatures with the corresponding circuit model used to fit the impedance data are shown in Fig. S12.

$Na_2B_{11}H_{13}$ presents an ionic conductivity of 2.5 x 10^{-7} S cm^{-1} at 30 °C with a sudden increase upon heating, reaching 2.9 x 10^{-3} S cm^{-1} at 100 °C, a similar result to that observed for Na *β*-Al_2O_3 and $NaB_{11}H_{14}\cdot(H_2O)_n$ at the same temperature (≈ 1 x 10^{-2} S cm^{-1}). This step-function type behaviour is similar to the results observed for the *nido*-boranes Na-7,8-$C_2B_9H_{12}$ and Na-7-$CB_{10}H_{13}$,[27] and the *closo*-borane $Na_2B_{10}H_{10}$[14] as they undergo an order-disorder polymorphic transition with temperature increase. Even though $Na_2B_{11}H_{13}$ assumes a disordered *bcc* structure as $NaB_{11}H_{14}$ (space group *I*$\bar{4}$3*d*) at high temperature,[27] the Na^+ conductivity observed for the former is 7.7 x 10^{-3} S cm^{-1} at 200 °C, whereas the latter exhibits results in the order of 10^{-2} S cm^{-1} at 100 °C. The lower ionic conductivity observed for $Na_2B_{11}H_{13}$ compared to $NaB_{11}H_{14}$ may be a result of the reduced number of vacant sites for cation hopping, since despite having a similarly sized unit cell, $Na_2B_{11}H_{13}$ has twice the number of Na^+ ions in its structure for charge-balance. There is also an increased Coulombic attraction between divalent anions, as in $B_{11}H_{13}^{2-}$, and Na^+, as opposed to monovalent $B_{11}H_{14}^{-}$, which may also reduce cationic conductivity in $Na_2B_{11}H_{13}$.[27,65] Despite this, the ionic conductivity observed in $Na_2B_{11}H_{13}$ is significantly higher than either $Na_2B_{12}H_{12}$,[63] $NaBH_4$[62] and $Na_2B_{12}Cl_{12}$[41] in the temperature range of 30 – 200 °C (Fig. 6). The $B_{11}H_{13}^{2-}$ anion exhibits an asymmetric charge distribution (or polarisation), which is analogous to other *nido*-boranes as well as carboranes, such as $CB_9H_{10}^{-}$, which have interesting reorientational dynamics governed by their charge polarity.[65] In contrast, $Na_2B_{12}H_{12}$[63] contains an isotropic *closo*-borane anion, which yields a salt with lower ionic conductivity.[27]

The activation energy (E_a) for Na^+ conduction for LT $Na_2B_{11}H_{13}$ was measured to be 0.73 eV (± 0.02 eV). This is similar to other sodium *nido*-boranes, such as Na-7-$CB_{10}H_{13}$, Na-7,8-$C_2B_9H_{12}$ and $NaB_{11}H_{14}$,[27] which demonstrate an E_a of 0.68, 0.78 and 0.61 eV, respectively, for Na^+ ion conduction in their low temperature ordered crystallographic phases (Table S1). Upon the order-disorder polymorphic transition the E_a for Na^+ conductivity in $Na_2B_{11}H_{13}$ decreases to 0.36 (± 0.03 eV) eV, which is within the range for other disordered high temperature sodium boranes, such as Na-7-$CB_{10}H_{13}$ (0.42 eV),[27] Na-7,8-$C_2B_9H_{12}$ (0.39 eV),[27] $NaB_{11}H_{14}$ (0.41 eV),[27] $Na_2B_{10}H_{10}$ (0.47 eV),[14] and $Na_2B_{12}H_{12}$ (0.21 eV)[63] (Table S1).

Mixed-anion $Na_{11}(B_{11}H_{14})_3(B_{11}H_{13})_4$ presents higher Na^+ conductivity than the LT $Na_2B_{11}H_{13}$ and $NaB_{11}H_{14}$,[27] which shows that the formation of the solid-solution results in a material with better ionic conductivity properties near room temperature (4.6 x 10^{-5} S cm^{-1} at 30 °C) than its constituents (Fig. S11). The results of Na^+ conductivity for $Na_{11}(B_{11}H_{14})_3(B_{11}H_{13})_4$ from 100 – 170 °C are also close to that observed for the HT $Na_2B_{11}H_{13}$ (Fig. S11), with the mixed-anion solid-solution reaching an ionic conductivity of 3.0 x 10^{-3} S cm^{-1} at 170 °C, and $Na_2B_{11}H_{13}$ exhibiting a result of 6.1 x 10^{-3} S cm^{-1} at the same temperature. Again, this is thought to be related to the presence of the *Pm*$\bar{3}$*n* polymorph in the $Na_{11}(B_{11}H_{14})_3(B_{11}H_{13})_4$ structure at RT (Figs. 5 & S8). The stabilisation of the disordered superionic structure at RT via formation of mixed-borane-anion solid-solution has been previously seen as in $Na_2(CB_9H_{10})(CB_{11}H_{12})$[22] and $Na_2(B_{12}H_{12})_{0.5}(B_{10}H_{10})_{0.5}$.[23] The mixture of monovalent with divalent hydridoborate species, such as $Na_3(BH_4)(B_{12}H_{12})$,[64] $Na_4(B_{11}H_{14})_2(B_{12}H_{12})$,[29] $Na_4(CB_{11}H_{12})_2(B_{12}H_{12})$,[31] and

This journal is © The Royal Society of Chemistry 20xx

Please do not adjust margins

Please do not adjust margins

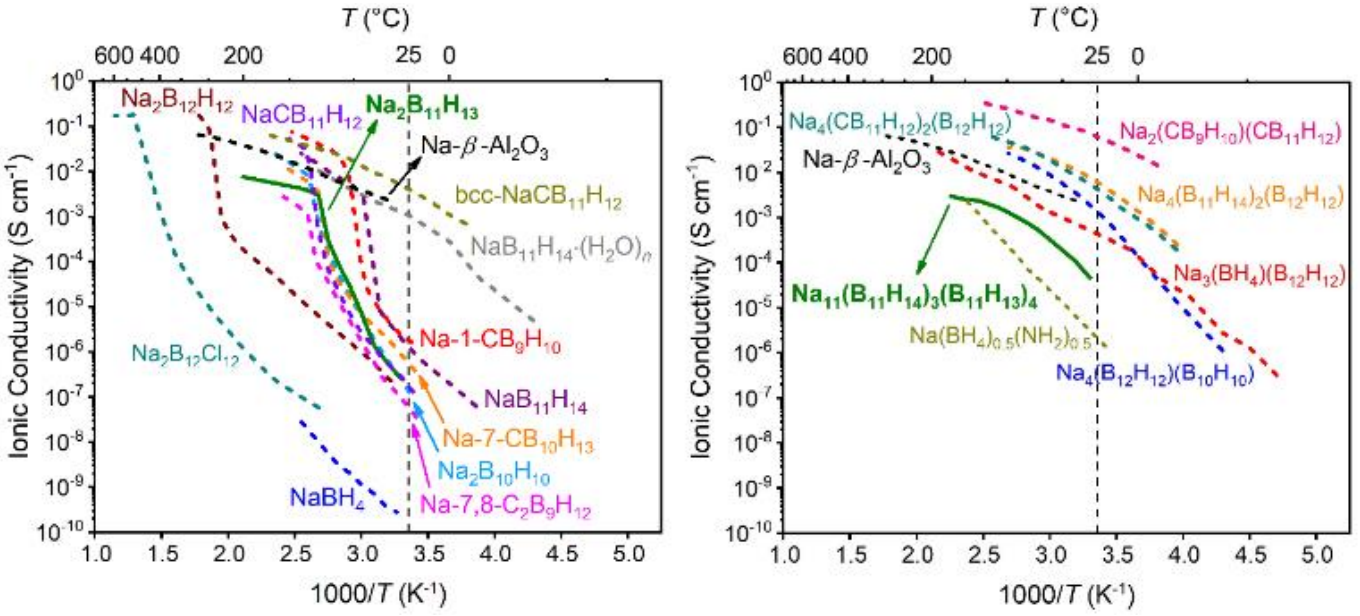

Fig. 6. Solid-state ionic conductivity of $Na_2B_{11}H_{13}$ and $Na_{11}(B_{11}H_{14})_3(B_{11}H_{13})_4$ as a function of temperature compared to other sodium single anion (left)[11,12,14,15,27,29,41,62,63] and mixed anion (right)[20,21,26,28,65,67] hydridoborate materials. bcc-$NaCB_{11}H_{12}$ represents the ionic conductivity of the mechanically-milled $NaCB_{11}H_{12}$, which presents a body-centered cubic (bcc) polymorph at RT.[19] The solid-state electrolyte Na-β-Al_2O_3 was also added for comparison in both plots.[1] The solid green lines denote the ionic conductivity of the samples synthesised in the present work.

$Na_3(NH_2)(B_{12}H_{12})$[66] has also already been presented as an efficient strategy to enhance the ionic conductivity properties of the material. The result observed for the Na^+ conductivity of $Na_{11}(B_{11}H_{14})_3(B_{11}H_{13})_4$ near room temperature is also higher than the majority of the single-anion sodium-borane compounds reported so far at the same temperature (Fig. 6) and presents lower ionic conductivity when compared to $NaB_{11}H_{14}\cdot(H_2O)_n$ (1.1 x 10^{-3} S cm^{-1} at 25 °C) as water may facilitate the Na^+ migration (Fig. S11),[11] and to bcc-$NaCB_{11}H_{12}$ (4 x 10^{-3} S cm^{-1} at 25 °C) as mechanical modification induces stabilisation of the bcc polymorph at RT.[19]

The activation energy for Na^+ conductivity in $Na_{11}(B_{11}H_{14})_3(B_{11}H_{13})_4$ was measured to be 0.51 eV (± 0.02 eV) from 30 – 80 °C, which lies between the results observed for the HT and the LT $Na_2B_{11}H_{13}$ and $NaB_{11}H_{14}$ (Table S1).

Fig. 6 also shows that the mixture $Na_{11}(B_{11}H_{14})_3(B_{11}H_{13})_4$ presents higher ionic conductivity results than $Na(BH_4)_{0.5}(NH_2)_{0.5}$ in the temperature range of 30 – 170 °C,[62] yet lower results when compared to other mixed-anion solid solutions. However, the synthesis of $Na_{11}(B_{11}H_{14})_3(B_{11}H_{13})_4$ reported here requires only the use of wet chemistry approaches and common laboratory consumables, which may be more cost-effective than when compared to the majority of the syntheses reported for carboranes.[67]

The oxidative stability limit of $Na_2B_{11}H_{13}$ was determined to be 2.1 V against Na metal based on the anodic peak observed in its linear sweep voltammogram at 30 °C (Fig. S13). This result is similar to the one determined for $NaBH_4$ (1.9 V vs. Na^+/Na)[68,69] and higher than the oxidative stability limit estimated for $Li_2B_{11}H_{13}$ against Li metal (< 1.0 V), which was based on DFT calculations.[28] However, the oxidative stability limit of $Na_2B_{11}H_{13}$ is lower than the ones for $NaB_{11}H_{14}$[29] and $NaB_{11}H_{14}\cdot(H_2O)_n$[11] with both exhibiting an onset of decomposition at 2.6 V vs. Na^+/Na. The mixed-anion $Na_{11}(B_{11}H_{14})_3(B_{11}H_{13})_4$ exhibited two onsets of anodic current, one at 2.1 V and another one at ≈ 2.7 V (Fig. S13), which is in agreement with the electrochemical decomposition of $Na_2B_{11}H_{13}$ and $NaB_{11}H_{14}$, respectively. A multistep oxidation process has been reported for other mixed-anion boranes, such as $Na_4(B_{12}H_{12})(B_{10}H_{10})$, which presents two onsets of decomposition, one at 3.02 V vs. Na^+/Na and another one at 3.22 V vs. Na^+/Na that were attributed to $Na_2B_{10}H_{10}$ and $Na_2B_{12}H_{12}$, respectively.[43]

The higher electrochemical stability of *closo*-boranes, such as $Na_2B_{10}H_{10}$ and $Na_2B_{12}H_{12}$, than *nido*-boranes, as in $NaB_{11}H_{14}$ and $Na_2B_{11}H_{13}$, can be expected as the latter present an open borane cage with delocalised hydrogen atoms, which tend to reduce their stability, with hydrogen release or dimer formation upon oxidation.[29] Despite that, an oxidative stability limit of 2.1 V vs. Na^+/Na, as in samples of $Na_2B_{11}H_{13}$, may not be an issue for their application as solid-state electrolytes in Na-S batteries as such batteries present a working potential in the range of 1.78 – 2.08 V.[37,70] Besides that, the use of Na as the anode in solid-state batteries brings additional challenges that may need to be overcome prior to practical applications. For example, pure Na-metal can lead the battery to short circuit due to Na dendrite formation,[71] and the use of a Na-Sn alloy as the anode can result in battery capacity fade owing to the volume expansion of Sn.[72] Therefore, the compatibility of sodium-borane electrolytes, such as $Na_2B_{11}H_{13}$, $NaB_{11}H_{14}$, $NaB_{11}H_{14}\cdot(H_2O)_n$, and $Na_{11}(B_{11}H_{14})_3(B_{11}H_{13})_4$, should also be assessed against other types of anode materials, for instance, hard carbon and $Na_2Ti_3O_7$.[73–75]

Conclusions

A facile synthesis of the solid-state $Na_2B_{11}H_{13}$ and the mixed-anion solid-solution $Na_{11}(B_{11}H_{14})_3(B_{11}H_{13})_4$ was reported.

Please do not adjust margins

Please do not adjust margins

$Na_2B_{11}H_{13}$ undergoes a polymorphic phase change at ≈ 170 °C assuming a body-centered cubic structure indexed in $Pm\overline{3}n$, isostructural to the first HT phase observed for $Na_2B_{12}H_{12}$. Even though both $Na_2B_{11}H_{13}$ and $NaB_{11}H_{14}$ assume a bcc polymorph at HT, the latter presents higher Na^+ conductivity than the former, with $Na_2B_{11}H_{13}$ reaching 7.7 x 10^{-3} S cm^{-1} at 200 °C. It is proposed that the increased Coulombic attraction between Na^+ and divalent $B_{11}H_{13}^{2-}$, along with the increased cation site occupancy, decreases the mobility of the cation in the crystal structure compared to the monovalent $B_{11}H_{14}^-$ analogue.

At 30 °C, $Na_{11}(B_{11}H_{14})_3(B_{11}H_{13})_4$ exhibits an ionic conductivity (4.7 x 10^{-5} S cm^{-1}) higher than its constituents $NaB_{11}H_{14}$ (2 x 10^{-6} S cm^{-1}) and $Na_2B_{11}H_{13}$ (2.5 x 10^{-7} S cm^{-1}). XRPD data for $Na_{11}(B_{11}H_{14})_3(B_{11}H_{13})_4$ shows the disordered $Pm\overline{3}n$ polymorph at RT, which is observed for $Na_2B_{11}H_{13}$ at high temperatures. This shows that a mixed-anion solid-solution could partially stabilise the HT disordered-polymorph at RT, which results in a sample with increased ionic conductivity properties.

$Na_2B_{11}H_{13}$ presents higher thermal stability than $NaB_{11}H_{14}$, however the former is more susceptible to voltage induced oxidation against Na metal, with an oxidative stability limit of 2.1 V vs. Na^+/Na at 30 °C compared to 2.6 V vs. Na^+/Na for $NaB_{11}H_{14}$ or $NaB_{11}H_{14}\cdot(H_2O)_n$ at same temperature. $Na_{11}(B_{11}H_{14})_3(B_{11}H_{13})_4$ exhibits two onsets of electrochemical decomposition at 2.1 V and 2.7 V vs. Na^+/Na at 30 °C, which are in agreement with the oxidative stability limit observed for its counterparts. Sodium *nido*-boranes show great potential as solid-state ion conductors and should be implemented in all-solid-state battery cells in the near future to assess their performance against promising anode and cathode materials.

Conflicts of interest

There are no conflicts to declare.

Acknowledgements

DHPS acknowledges the support from Curtin-ATN South American Scholarship and Tuition Fee-Offset Scholarship through Curtin University. The authors thank Gareth Nealon for his help in solid-state NMR data collection. CEB, MP, and TDH acknowledge the financial support of the Global Innovation Linkage (GIL73589). CEB acknowledges the financial support of the ARC for the LIEF grant LE170100199. This research was undertaken on the Powder Diffraction beamline at the Australian Synchrotron, part of ANSTO.

References

1 B. R. S. Hansen, M. Paskevicius, H. Li, E. Akiba and T. R. Jensen, Coord. Chem. Rev., 2016, 323, 60–70.
2 R. Černý, F. Murgia and M. Brighi, J. Alloys Compd., 2022, 895, 162659.
3 F. Ali, N. S Hosmane and Y. Zhu, Molecules, 2020, 25, 1–24.
4 J. D. Clark, Ignition!: An Informal History of Liquid Rocket Propellants, Rutgers University Press, New Brunswick, 1972.
5 C. Faverio, M. F. Boselli, F. Medici and M. Benaglia, Org. Biomol. Chem., 2020, 18, 7789–7813.
6 J. Michel, B. Faure and M. Ma, Coord. Chem. Rev., 1998, 178–180, 665–698.
7 L. H. Rude, T. K. Nielsen, D. B. Ravnsbæk, U. Bo, M. B. Ley, B. Richter, L. M. Arnbjerg, M. Dornheim, Y. Filinchuk and F. Besenbacher, Phys. Status Solidi A, 2011, 208, 1754–1773.
8 H. Hagemann, Molecules, 2021, 26, 7425.
9 C. Frommen, M. H. Sørby, M. Heere, T. D. Humphries, J. E. Olsen and B. C. Hauback, Energies, 2017, 10, 2115.
10 D. B. Ravnsbæk, Y. Filinchuk and M. Dornheim, Chem. Soc. Rev, 2017, 46, 1565–1634.
11 D. H. P. Souza, K. T. Møller, S. A. Moggach, T. D. Humphries, A. M. D'Angelo, C. E. Buckley and M. Paskevicius, J. Mater. Chem. A, 2021, 9, 15027–15037.
12 W. S. Tang, A. Unemoto, W. Zhou, V. Stavila, M. Matsuo, H. Wu, S. Orimo and T. J. Udovic, Energy Environ. Sci., 2015, 8, 3637–3645.
13 M. Paskevicius, B. R. S. Hansen, M. Jørgensen, B. Richter and T. R. Jensen, Nat. Commun., 2017, 8, 10–15.
14 T. J. Udovic, M. Matsuo, W. S. Tang, H. Wu, V. Stavila, A. V Soloninin, R. V Skoryunov, O. A. Babanova, A. V Skripov, J. J. Rush, A. Unemoto, H. Takamura and S. Orimo, Adv. Mater., 2014, 26, 7622–7626.
15 W. S. Tang, M. Matsuo, H. Wu, V. Stavila, W. Zhou, A. A. Talin, A. V Soloninin, R. V Skoryunov, O. A. Babanova, A. V Skripov, A. Unemoto, S.-I. Orimo and T. J. Udovic, Adv. Energy Mater., 2016, 6, 1502237.
16 T. A. Dobbins, Molecules, 2021, 26, 3239.
17 A. Gradisek, M. Jørgensen, M. Paskevicius, B. R. S. Hansen and T. R. Jensen, J. Phys. Chem. C, 2021, 125, 5534–5541.
18 Y. Sadikin, P. Schouwink, M. Brighi, Z. Łodziana and R. Černý, Inorg. Chem., 2017, 56, 5006–5016.
19 F. Murgia, M. Brighi, L. Piveteau, C. E. Avalos, V. Gulino, M. C. Nierstenh, P. Ngene, P. De Jongh and C. Radovan, ACS Appl. Mater. Interfaces, 2021, 13, 61346–61356.
20 S. Kim, N. Toyama, H. Oguchi, T. Sato, S. Takagi, T. Ikeshoji and S. Orimo, Chem. Mater., 2018, 30, 386–391.
21 W. S. Tang, M. Matsuo, H. Wu, V. Stavila, A. Unemoto, S. I. Orimo and T. J. Udovic, Energy Storage Mater., 2016, 4, 79–83.
22 W. S. Tang, K. Yoshida, A. V. Soloninin, R. V. Skoryunov, O. A. Babanova, A. V. Skripov, M. Dimitrievska, V. Stavila, S. I. Orimo and T. J. Udovic, ACS Energy Lett., 2016, 1, 659–664.
23 L. Duchêne, R. S. Kühnel, D. Rentsch, A. Remhof, H. Hagemann and C. Battaglia, Chem. Commun., 2017, 53, 4195–4198.
24 M. Brighi, F. Murgia, Z. Łodziana, P. Schouwink, A. Wołczyk and R. Černý, J. Power Sources, 2018, 404, 7–12.
25 Y. S. Choi, Y. S. Lee, D. J. Choi, K. H. Chae, K. H. Oh and Y. W. Cho, J. Phys. Chem. C, 2017, 121, 26209–26215.
26 V. Gulino, L. Barberis, P. Ngene, M. Baricco and P. E. De Jongh, ACS Appl. Energy Mater., 2020, 3, 4941–4948.
27 W. S. Tang, M. Dimitrievska, V. Stavila, W. Zhou, H. Wu, A. A. Talin and T. J. Udovic, Chem. Mater., 2017, 29, 10496–10509.
28 S. H. Payandeh, D. Rentsch, Z. Łodziana, R. Asakura, L. Bigler, R. Černý, C. Battaglia and A. Remhof, Adv. Funct. Mater., 2021, 31, 2010046.
29 S. Payandeh, R. Asakura, P. Avramidou, D. Rentsch, Ł. Zbigniew, C. Radovan, A. Remhof and C. Battaglia, Chem. Mater., 2020, 32, 1101–1110.
30 S. Kim, H. Oguchi, N. Toyama, T. Sato, S. Takagi, T. Otomo, D. Arunkumar, N. Kuwata, J. Kawamura and S. Orimo, Nat. Commun., 2019, 10, 1–9.
31 R. Asakura, D. Reber, L. Duchêne, S. Payandeh, A. Remhof, H. Hagemann and C. Battaglia, Energy Environ. Sci., 2020, 13, 5048–5058.
32 F. Murgia, M. Brighi and R. Černý, Electrochem. commun., 2019, 106, 106534.
33 R. Kurmelovs, 'Gone ballistic': lithium price rockets nearly 500% in a year amid electric vehicle rush,

This journal is © The Royal Society of Chemistry 20xx

Please do not adjust margins

Please do not adjust margins

https://www.theguardian.com/australia-news/2022/feb/09/gone-ballistic-lithium-price-rockets-nearly-500-in-a-year-amid-electric-vehicle-rush, (accessed 5 May 2022).
34 S. Yang, F. Zhang, H. Ding, P. He and H. Zhou, Joule, 2018, 2, 1648–1651.
35 B. L. Ellis and L. F. Nazar, Curr. Opin. Solid State Mater. Sci., 2012, 16, 168–177.
36 Y. Zhao, K. R. Adair and X. Sun, Energy Environ. Sci., 2018, 11, 2673–2695.
37 S. Xin, Y. X. Yin, Y. G. Guo and L. J. Wan, Adv. Mater., 2014, 26, 1261–1265.
38 J. He, A. Bhargav, W. Shin and A. Manthiram, J. Am. Chem. Soc., 2021, 143, 20241–20248.
39 A. Bergamaschi, A. Cervellino, R. Dinapoli, F. Gozzo, B. Henrich, I. Johnson, P. Kraft, A. Mozzanica, B. Schmitt and X. Shi, J. Synchrotron Radiat., 2010, 17, 653–668.
40 A. A. Coelho, J. Appl. Crystallogr., 2018, 51, 210–218.
41 B. R. S. Hansen, M. Paskevicius, M. Jørgensen and T. R. Jensen, Chem. Mater., 2017, 29, 3423–3430.
42 A. Gradišek, M. Krnel, M. Paskevicius, B. R. S. Hansen, T. R. Jensen and J. Dolinšek, J. Phys. Chem. C, 2018, 122, 17073–17079.
43 R. Asakura, L. Duchêne, R. S. Kühnel, A. Remhof, H. Hagemann and C. Battaglia, ACS Appl. Energy Mater., 2019, 2, 6924–6930.
44 A. Hepp, R. Labbow, F. Reiß, A. Schulz and A. Villinger, Eur. J. Inorg. Chem., 2018, 2018, 2905–2914.
45 J. Pecyna, I. Rončević and J. Michl, Molecules, 2019, 24, 3779.
46 M. Wang, L. Ouyang, M. Zeng, J. Liu, C. Peng, H. Shao and M. Zhu, Int. J. Hydrogen Energy, 2019, 44, 7392–7401.
47 X. Luo, Master Thesis, University of New South Wales, 2019.
48 D. Schubert, in Kirk-Othmer Encyclopedia of Chemical Technology, 2011, pp. 1–68.
49 M. R. Hansen, G. K. H. Madsen, H. J. Jakobsen and J. Skibsted, J. Phys. Chem. A, 2005, 109, 1989–1997.
50 M. R. Hansen, T. Vosegaard, H. J. Jakobsen and J. Skibsted, J. Phys. Chem. A, 2004, 108, 586–594.
51 S. Kroeker and J. F. Stebbins, Inorg. Chem., 2001, 40, 6239–6246.
52 B. Liu, A. Rose, N. Zhang, Y. Y. Hu and M. Ma, J. Phys. Chem. C, 2017, 121, 12610–12616.
53 C. Lang, Y. Jia, J. Liu, H. Wang, L. Ouyang, M. Zhu and X. Yao, Int. J. Hydrogen Energy, 2017, 42, 13127–13135.
54 M. Bishop, N. Shahid, J. Yang and A. R. Barron, Dalt. Trans., 2004, 2621–2634.
55 R. K. Momii and N. H. Nachtrieb, Inorg. Chem., 1967, 6, 1189–1192.
56 M. Paskevicius, M. P. Pitt, C. J. Webb, D. A. Sheppard, U. Filsø, E. M. Gray and C. E. Buckley, J. Phys. Chem. C, 2012, 116, 15231–15240.
57 H. E. Gottlieb, G. Graczyk-Millbrandt, G. G. A. Inglis, A. Nudelman, D. Perez, Y. Qian, L. E. Shuster, H. F. Sneddon and R. J. Upton, Green Chem., 2016, 18, 3867–3878.
58 H. E. Gottlieb, V. Kotlyar and A. Nudelman, J. Org. Chem., 1997, 62, 7512–7515.
59 N. Verdal, J. H. Her, V. Stavila, A. V. Soloninin, O. A. Babanova, A. V. Skripov, T. J. Udovic and J. J. Rush, J. Solid State Chem., 2014, 212, 81–91.
60 W. Dirk and P. Paetzold, Z. Anorg. Allg. Chem., 2001, 627, 2615–2618.
61 O. Volkov and P. Paetzold, J. Organomet. Chem., 2003, 680, 301–311.
62 M. Matsuo, S. Kuromoto, T. Sato, H. Oguchi, H. Takamura and S. I. Orimo, Appl. Phys. Lett., 2012, 100, 2–6.
63 T. J. Udovic, M. Matsuo, A. Unemoto, N. Verdal, V. Stavila, A. V. Skripov, J. J. Rush, H. Takamura and S. I. Orimo, Chem. Commun., 2014, 50, 3750–3752.
64 Y. Sadikin, M. Brighi, P. Schouwink and R. Černý, Adv. Energy Mater., 2015, 5, 1501016.
65 A. V. Soloninin, M. Dimitrievska, R. V. Skoryunov, O. A. Babanova, A. V. Skripov, W. S. Tang, V. Stavila, S. I. Orimo and T. J. Udovic, J. Phys. Chem. C, 2017, 121, 1000–1012.
66 L. He, H. Lin, H. F. Li, Y. Filinchuk, J. Zhang, Y. Liu, M. Yang, Y. Hou, Y. Deng, H. W. Li, H. Shao, L. Wang and Z. Lu, J. Power Sources, 2018, 396, 574–579.
67 A. Berger, C. E. Buckley and M. Paskevicius, Inorg. Chem., 2021, 60, 14744–14751.
68 V. Lacivita, Y. Wang, S. H. Bo and G. Ceder, J. Mater. Chem. A, 2019, 7, 8144–8155.
69 Z. Lu and F. Ciucci, Chem. Mater., 2017, 29, 9308–9319.
70 Z. Wen, Y. Hu, X. Wu, J. Han and Z. Gu, Adv. Funct. Mater., 2013, 23, 1005–1018.
71 B. Lee, E. Paek, D. Mitlin and S. W. Lee, Chem. Rev., 2019, 119, 5416–5460.
72 L. Duchêne, D. H. Kim, Y. B. Song, S. Jun, R. Moury, A. Remhof, H. Hagemann, Y. S. Jung and C. Battaglia, Energy Storage Mater., 2020, 26, 543–549.
73 K. Niitani, S. Ushiroda, H. Kuwata, H. N. Ohata, Y. Shimo, M. Hozumi, T. Matsunaga and S. Nakanishi, ACS Energy Lett., 2022, 7, 145–149.
74 C. Zhou, S. Bag and V. Thangadurai, ACS Energy Lett., 2018, 3, 2181–2198.
75 R. P. Rao, H. Chen, L. L. Wong and S. Adams, J. Mater. Chem. A, 2017, 5, 3377–3388.

Please do not adjust margins